Widely Distributed Radar Imaging: Unmediated ADMM Based Approach

Ahmed Murtada, Ruizhi Hu, Bhavani Shankar Mysore Rama Rao, Udo Schroeder

***Abstract*—This paper presents a novel approach to reconstruct a unique image of an observed scene via synthetic apertures (SA) generated by employing widely distributed radar sensors. The problem is posed as a constrained optimization problem in which the global image which represents the aggregate view of the sensors is a decision variable. While the problem is designed to promote a sparse solution for the global image, it is constrained such that a relationship with local images that can be reconstructed using the measurements at each sensor is respected. Two problem formulations are introduced by stipulating two different establishments of that relationship. The proposed formulations are designed according to consensus ADMM (CADMM) and sharing ADMM (SADMM), and their solutions are provided accordingly as iterative algorithms. We drive the explicit variable updates for each algorithm in addition to the recommended scheme for hybrid parallel implementation on the distributed sensors and a central processing unit. Our algorithms are validated and their performance is evaluated by exploiting the Civilian Vehicles Dome dataset to realize different scenarios of practical relevance. Experimental results show the effectiveness of the proposed algorithms, especially in cases with limited measurements.**

***Index Terms*—Radar Imaging, Widely distributed radars, Synthetic Aperture, Wide angle SAR, ADMM.**

I. Introduction

Widely distributed radar systems are robust and fault-tolerant systems that provide high angular resolution and permit the exploitation of spatial diversity and occlusion avoidance [1]. They may also be viewed as synthesizing wide aperture in the spatial domain [2]. The emergence of commercial off-the-shelf (COTS) mmWave radar modules with wide bandwidths in excess of 4 GHz enables such a synthetic aperture (SA) using spatially well-separated modules. With applications in surveillance, assisted living, and health monitoring, radar systems with distributed antennas are expected to play a vital role in emerging sensing paradigms [3], [4]. Under this architecture, the observed targets feature an aspect-dependent scattering behavior restricting the employment of conventional imaging methods. The main impediment arises due to the adoption of the isotropic point scattering model of targets, thereby preventing algorithms like back-projection (BP) to provide an adequate imaging performance [5].

The problem of radar imaging with widely distributed sensors has not received enough attention in the literature. The works [6]–[8] considered radar imaging with distributed antennas and the related issues due to ambiguity in antenna positions and clocks synchronization. In these works, model-based optimization algorithms are utilized to jointly achieve the imaging task and resolve such issues. However, in these works, an isotropic scattering model, suitable when antennas are closely spaced, is assumed; this is clearly not suitable when widely separated antennas are considered.

On the other hand, in wide-angle synthetic aperture radars (WSAR), which bear a close resemblance to a widely distributed architecture, two approaches exist for imaging [9]. The first approach includes methods that utilize the full aperture data jointly. It encompasses the methods that are based on parametric modeling that characterizes the canonical scattering behavior of scatterers [10]–[13]. Correspondingly, the scene image is reconstructed through joint processing of the measurements from the whole aperture exploiting the model. Nevertheless, the imaging involves a dictionary search process that is computationally cumbersome [14].

The second approach is composite imaging [15]–[18] in which the full aperture is divided into sub-apertures within which the point scattering model holds. At first, images of each sub-aperture are formed through regularized optimization exploiting specific features such as sparsity and smoothness. Subsequently, individual images are fused to constitute an aggregate image of the scene through simple techniques such as the generalized likelihood ratio test (GLRT). This approach does not fully exploit the information from different aspects where the final image of the scene is only a fused version of the images reconstructed with sub-aperture data. Among other sub-aperture methods, dynamic compressive sensing (DCS) [19]–[22] aims to exploit the evolution of the scattering behavior structure along with the common sparse structure of sub-aperture images. These methods estimate a sequence of images and also do not attempt to reconstruct a single image; this has been referred to as a drawback in [23]. Moreover, they are heavily reliant on the assumptions of joint sparsity with highly overlapping support among sub-apertures and a gradual change of such a support [19], [21] − [23]. These assumptions are severely violated when views and/or bandwidth is limited. Additionally, since those methods require either processing the entire data sequentially or jointly, an efficient parallel implementation becomes difficult to realize [9].

While we also propose a sub-aperture method, unlike composite imaging, we aim to solve the problem of widely distributed radar imaging by directly reconstructing a global image that is introduced as an aggregate view of the scene. Besides, the prior information is only imposed on the global

This work is supported by Luxembourg National Research Fund (FNR) through the Industrial Fellowship grant IF/15364040/RADII.

A. Murtada, R. Hu, and B.S.M. Rama Rao are with the Interdisciplinary Centre for Security, Reliability and Trust (SnT), University of Luxembourg, L1885 Luxembourg City, Luxembourg (e-mail: ahmed.murtada@uni.lu; ruizhi.hu@uni.lu; bhavani.shankar@uni.lu). U. Schroeder is with IEE S.A., L-7795 Bissen, Luxembourg (email: Udo.schroeder@iee.lu).

image rather than the local images of individual sensors. Concurrently, the correspondence between the local images and the global one is defined as a constraint to the optimization problem. Our approach allows for better data exploitation by including the global image as a decision variable in the optimization problem. We then provide a solution based on the alternating direction method of multipliers (ADMM) framework [24]. ADMM is a powerful distributed optimization regime suitable for systems that incorporate a collection of measurements through a distributed architecture. In [25] and [26], ADMM has been introduced as a fast reconstruction method for generic imaging inverse problems. Further, in [27] it is applied to reconstruct complex SAR images with enhanced features in particular and to perform imaging with under-sampled measurements in the presence of phase errors in [28].

While in these works ADMM has been mainly utilized to facilitate the solution of a non-constrained optimization problem by the virtue of variable splitting, we employ its constrained formulation directly in the interest of exploiting the system architecture and implementing parallelizable image reconstruction algorithms. Accordingly, we establish two problem formulations inspired by consensus ADMM (CADMM) and sharing ADMM (SADMM). The first formulation comes as a generalization of our previous work [29] in which CADMM is utilized to mitigate the layover artifacts in widely distributed radar imaging by considering sub-aperture measurements from different elevations. While CADMM imposes a consensus on all sub-images, albeit under an anisotropic setting, we present CADMM as a low complexity initial work that introduces the association between sub-aperture images and the global image, and reconstructs the image of the scene without restriction on data viewing angles. Moreover, by stipulating the more relaxed sharing association in the constraints, we introduce the second problem formulation based on SADMM. The different association introduced by SADMM formulation enables another exploitation of the relationship between the data collected by the sub-apertures. Additionally, it provides an alternative realization of the system architecture through the ensuing unalike solution. We provide the solutions as iterative algorithms with a recommendation of a parallel implementation paradigm. Finally, the Civilian Vehicles Dome dataset [30] is used to realize three experiments that comprise different practical use cases. Through them, we validate our algorithms and show the performance of CADMM and SADMM, where the latter is found to provide an enhanced imaging performance in most of the scenarios.

The contribution of this paper lies in the introduction of a parallelizable distributed optimization framework to reconstruct an image of a scene observed by widely distributed radar apertures without the need for an explicit later fusion step. The proposed framework allows the adoption of any prior information about the observed scene in addition to giving the liberty to stipulate the relation between the global image and the measurements collected by individual apertures. Moreover, validate the proposed approach by exploiting the prior information on the sparsity of the global image and establishing the consensus and sharing relationships between global and local images. Our proposed approach is well-adapted for implementation on various architectures including WSAR and radar systems with collocated antennas.

Throughout this paper, vectors are denoted by lowercase bold font, while matrices are in uppercase bold. $\mathbf{I}_L$ is the identity matrix of size $L \times L$ and $\mathbf{1}_N$ is a vector of all ones of size $N \times 1$. The superscripts $.^T$ and $.^H$ denote, respectively, the transpose and the complex conjugate transpose of a vector or a matrix. On the other hand, superscripts in parentheses denote the iteration count. The symbol $\otimes$ is used for the Kronecker product.

II. Signal Model and Background

In this section, we present the considered distributed architecture, introduce the adopted signal model and provide background about the imaging problem formulation in the literature.

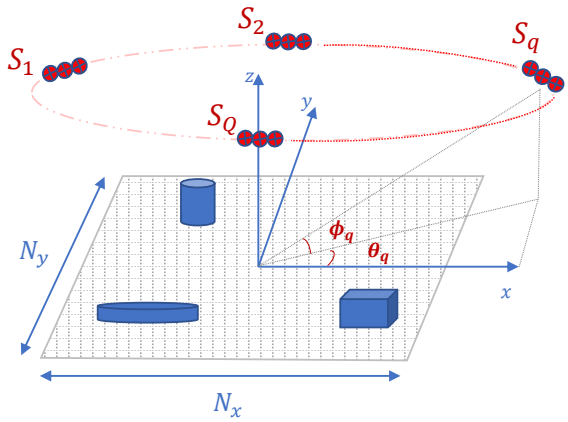

Fig. 1: Geometry of Distributed Radar System

Considering the system geometry illustrated in Fig. 1, a group of red crossed circles constitute a cluster of antenna phase centers (APCs). The figure shows the case we consider in our paper where each of the Q sensors forms a single cluster at identical elevation angles. We consider a mono-static configuration where each sensor receives the reflections due to its own illumination of the scene and does not process the reflections induced by transmissions from others. Accordingly, our proposed algorithms can be applied to architectures that are formed either by a synthetic or a real aperture. At each cluster, the isotropic scattering model of the targets in the scene is assumed. This way, the problem of aspect-dependant scattering behavior can be relaxed and Q local images can be formed by processing the measurements of individual clusters. The local images can then be appropriately combined at a central node, or the fusion center, to generate the image of the entire scene. The fusion center can subscribe to different combining methodologies, e.g., averaging or pixel-wise maximum, some of which will be explored in the sequel.

A. Tomography Inspired Modelling

Since the system comprises distributed sensors stationed at a diverse range of aspect angles and our goal is to form a

2D reflectivity image of the scene, we adopt the tomographic radar imaging framework [31] to describe the signal model. The tomographic model relies on the Projection-Slice Theorem (PST), a foundational result in computer tomography (CT) where a cross-section of an internal body part is imaged by detecting the attenuation of traversing X-rays. In a CT scan, the subject is exposed to a parallel beam of X-rays at a wide range of angles. At each angle, a row of detectors at the opposite side measures the attenuation by forming a projection profile of the intensity function of the imaged part along the emitting direction. PST (also known as Fourier-Slice Theorem) states that the one dimension (spatial) Fourier transform of a projection profile at an angle θ is equivalent to the 2D Fourier transform of the intensity function evaluated at a slice (line) that lies at the same angle θ in the spatial frequency domain. This result allows for direct inversion of the measured projections after taking a Fourier transform to reconstruct the desired intensity image.

Similarly, Radar imaging systems having a geometry that favors spatial diversity, have adopted the tomographic signal model for simpler interpretation and direct applicability of efficient tools such as the fast Fourier transform (FFT). Such systems include Spotlight-SAR and Circular-SAR, in addition to custom multistatic geometries [32]. However, the application of PST in radar imaging differs in some aspects with respect to CT due to the differences in both the acquisition method and the nature of the scattering to be recovered. In Radar imaging, the measured signal is a transformed version of a transmitted waveform, which is delayed in time and shifted in phase due to the location and proprieties of the scattering target. As a result, the measured quantity is not the projection of the scattering of the target as the case in CT *per-se*. Consequently, some restrictions, which are governed by the transmitted signal bandwidth, are imposed on the available spatial frequency samples. The frequency samples are located on an annulus centered around the carrier frequency with a width proportional to the signal bandwidth. However, effective image reconstruction from these limited portions is still possible using the frequency content of these sectors [33]. We refer the readers to [31]–[34] for additional background about the tomographic modelling of Radar imaging including its advantages and limitations.

B. Distributed Radar Imaging Model

We consider the sensors to transmit the commonly used linear frequency modulated (LFM) waveform with a chirp rate ν. Consequently, they receive a scaled and time-shifted version of the transmitted waveform as reflection from the scene. According to the aforementioned tomographic model, the discrete phase history received at the m^{th} antenna of the q^{th} sensor after dechirping and low-pass filtering follows

$$y_q^m(k) = \iint_{\Omega} \tilde{x}_q(x,y) \exp\left\{-j\frac{4\pi f_k}{c}\Delta R_q^m(x,y)\right\} dx\ dy$$
$$\Delta R_q^m(x,y) = \cos\varphi_q\left(x\cos\theta_{q,m} + y\sin\theta_{q,m}\right), \tag{1}$$

where $\Delta R_q^m(x,y)$ is the difference of the distances from the sensors to the scene center and to a ground target located at coordinates (x,y) assuming far-field scenario, $m = 1,\dots,M$ is the index of antenna elements within each cluster, $q = 1,\dots,Q$ is the index of a sensor/cluster, $k = 1,\dots,K$ is the index of fast-time samples, Ω is the ground footprint, which is assumed to be the same for all antennas, $\tilde{x}_q(x,y)$ indicates the complex reflectivity coefficient of a ground target at coordinates (x,y) with respect to the q^{th} cluster, $f_k = (f_c + 2\nu k T_s)$ denotes the linear transmitted frequency where f_c is the carrier frequency and T_s is the fast-time sampling period, c is the speed of light, φ_q is the elevation angle of the q^{th} cluster, and $\theta_{q,m}$ is the azimuth angle of the m^{th} antenna element of the q^{th} cluster.

By discretizing the scene with a uniform grid of $N = N_x \times N_y$ pixels $\{(x_n,y_n)\}_{n=1}^N$ and stacking $\left\{\left\{y_q^m(k)\right\}_{k=1}^K\right\}_{m=1}^M$ into a vector $\mathbf{y}_q$, the phase history measurements can be written in a matrix form as

$$\mathbf{y}_q = \mathbf{A}_q\tilde{\mathbf{x}}_q + \mathbf{w}_q \in \mathbb{C}^{KM\times 1}, \tag{2}$$

where $\mathbf{A}_q = \left[\boldsymbol{\alpha}_q^1, \boldsymbol{\alpha}_q^2, \cdots, \boldsymbol{\alpha}_q^N\right] \in \mathbb{C}^{KM\times N}$ is the system model based forward operator that its columns $\boldsymbol{\alpha}_q^n \in \mathbb{C}^{KM\times 1}$ take the form

$$\boldsymbol{\alpha}_q^n = \begin{bmatrix} \exp\{-j4\pi f_1\cos\varphi_q/c\,(x_n\cos\theta_{q,1} + y_n\sin\theta_{q,1})\} \\ \exp\{-j4\pi f_2\cos\varphi_q/c\,(x_n\cos\theta_{q,1} + y_n\sin\theta_{q,1})\} \\ \vdots \\ \exp\{-j4\pi f_K\cos\varphi_q/c\,(x_n\cos\theta_{q,1} + y_n\sin\theta_{q,1})\} \\ \vdots \\ \exp\{-j4\pi f_1\cos\varphi_q/c\,(x_n\cos\theta_{q,M} + y_n\sin\theta_{q,M})\} \\ \exp\{-j4\pi f_2\cos\varphi_q/c\,(x_n\cos\theta_{q,M} + y_n\sin\theta_{q,M})\} \\ \vdots \\ \exp\{-j4\pi f_K\cos\varphi_q/c\,(x_n\cos\theta_{q,M} + y_n\sin\theta_{q,M})\} \end{bmatrix}, \tag{3}$$

$\tilde{\mathbf{x}}_q \in \mathbb{C}^{N\times 1}$ is the vector containing the complex scattering coefficients of the entire scene with respect to the q^{th} cluster, and $\mathbf{w}_q \in \mathbb{C}^{KM\times 1}$ summarizes all errors including receiver and measurement noise as well as model imperfections.

C. State-of-the-art Problem Formulation

Composite imaging algorithms obtain local images utilizing the signal received at each cluster and subsequently fuse them into a global image. The scene size is usually much larger than the number of measurements $N >> KM$ and the imaging task is the inverse problem of (2) which, consequently, becomes ill-posed. Compressed sensing methods are commonly used to solve this inverse problem. Particularly, local images are obtained by solving Q regularized least square optimization problems for each cluster of the form

$$\hat{\mathbf{x}}_q = \arg\min_{\tilde{\mathbf{x}}_q}\left\{\|\mathbf{y}_q - \mathbf{A}_q\tilde{\mathbf{x}}_q\|_2^2 + h(\tilde{\mathbf{x}}_q)\right\}, \tag{4}$$

where $\hat{\mathbf{x}}_q$ is the estimated local image using the measurements $\mathbf{y}_q$ for $q = 1,\dots,Q$ and $h(\cdot)$ is a regularization function that imposes apriori information about local images. Different choices of regularization function $h(\cdot)$ exist to enhance some image features such as sparsity and smoothness, among others.

When $h(\cdot)$ is a separable function (e.g. l_1-norm), the Q problems can be represented as a single optimization problem in Q variables since the least squares term is naturally separable. Explicitly, the problem can be written as

$$\{\hat{\mathbf{x}}_1,\ldots,\hat{\mathbf{x}}_Q\} = \min_{\tilde{\mathbf{x}}_1,\tilde{\mathbf{x}}_2,\cdots,\tilde{\mathbf{x}}_Q} \sum_{q=1}^{Q} \left\{ \|\mathbf{y}_q - \mathbf{A}_q\tilde{\mathbf{x}}_q\|_2^2 + \|\tilde{\mathbf{x}}_q\|_1 \right\}. \tag{5}$$

The problem in (5) is an unconstrained regularized optimization problem that has been tackled through different optimization techniques in the literature. Finally, the image of the scene is obtained through a fusion step of the Q reconstructed images which can be as simple as a pixel-wise maximization among the Q local images.

As mentioned in the introduction, we alternatively reconstruct the global image of the scene by introducing its variable in the objective function and imposing the l_1-norm on it directly for a sparsity-driven solution. Simultaneously, the relationship between the global image and local images is defined as a constraint for our optimization problem. In the next section, based on the ADMM framework, we provide two alternative problem formulations along with their solutions.

III. ADMM Framework for Distributed Radar Imaging

ADMM is a powerful framework that renders itself amenable for optimization problems of distributed nature. It is a suitable tool to be utilized in a distributed radar system especially when the component sensors are equipped with some computation power capabilities. Although this computation power might be limited, it can be exploited to process some information in order to reduce the communication overhead and the computational burden at the central node. It also reduces latency as certain operations can already be performed in parallel at the nodes. Here, we first give a brief introduction of general ADMM formulation followed by our proposed reformulations of the problem in (5) according to the ADMM framework.

Consider the following constrained optimization problem with linear constraints over two separable functions in two variables $\mathbf{u}$ and $\mathbf{z}$

$$\begin{aligned} &\arg\min_{\mathbf{u},\mathbf{z}} f(\mathbf{u}) + g(\mathbf{z}) \\ &s.t. \quad \mathbf{G}\mathbf{u} + \mathbf{H}\mathbf{z} = \mathbf{c}, \end{aligned} \tag{6}$$

where $\mathbf{G}$, $\mathbf{H}$, and $\mathbf{c}$ are the matrices and vector of appropriate dimensions that establish the constraints on the variables $\mathbf{u}$ and $\mathbf{z}$. The augmented Lagrangian function of the above problem becomes

$$\mathcal{L}(\mathbf{u},\mathbf{z},\boldsymbol{\sigma}) = \left\{ \begin{array}{c} f(\mathbf{u}) + g(\mathbf{z}) + \langle \boldsymbol{\sigma}, \mathbf{G}\mathbf{u} + \mathbf{H}\mathbf{z} - \mathbf{c} \rangle \\ + \dfrac{\beta}{2} \|\mathbf{G}\mathbf{u} + \mathbf{H}\mathbf{z} - \mathbf{c}\|_2^2 \end{array} \right\} \tag{7}$$

where $\boldsymbol{\sigma}$ is the dual variable, β is the augmented Lagrangian parameter, and $\langle \cdot,\cdot \rangle$ denotes the inner product of vectors.

The ADMM solution to the above problem is obtained by iteratively minimizing the augmented Lagrangian function with respect to both the variables $\mathbf{u}$ and $\mathbf{z}$ in an alternating fashion in addition to updating the dual variable each iteration. Accordingly, after the k^{th} iteration, the ADMM variable updates consist of [24]

$$\begin{aligned} \mathbf{u}^{(k+1)} &:= \arg\min_{\mathbf{u}} \mathcal{L}\left(\mathbf{u}, \mathbf{z}^{(k)}, \boldsymbol{\sigma}^{(k)}\right) \\ \mathbf{z}^{(k+1)} &:= \arg\min_{\mathbf{z}} \mathcal{L}\left(\mathbf{u}^{(k)}, \mathbf{z}, \boldsymbol{\sigma}^{(k)}\right) \\ \boldsymbol{\sigma}^{(k+1)} &:= \boldsymbol{\sigma}^{(k)} + \beta\left(\mathbf{G}\mathbf{x}^{(k+1)} + \mathbf{H}\mathbf{z}^{(k+1)} - \mathbf{c}\right) \end{aligned} \tag{8}$$

Embracing ADMM framework, we propose two different formulations as alternatives to (5). Towards introducing the new formulations, we introduce the global image, which is a unified entity representative of the scene; this refers to the output of the fusion step mentioned in Section II. This global image can be interpreted and utilized based on the application. For example, for automatic target recognition (ATR) tasks, the global image provides a strong means to identify and classify targets. Similarly, the global image serves in detecting occluded targets or parts of the same target that are prone to self-occlusion.

By introducing a new variable $\mathbf{x}_\mathbf{G} \in \mathbb{R}^{N\times 1}$ representing the magnitude of the global image, both the formulations will have the same objective function of minimizing the sum of the least square terms with respect to local images, in addition to minimizing the l_1 norm of the global image. The formulations differ in the constraints which define the relationship between the global and local images. The optimization in imaging can be carried out on real variables by decoupling complex images into their corresponding magnitude and phase [16], [35]. Consequently, we consider the magnitude of the images as our optimization variables assuming that the phases are estimated in a previous step. Specifically, we assume that we have estimated $\boldsymbol{\Theta}_q \in \mathbb{C}^{N\times N}$, the diagonal matrix containing the phase of all pixels of local image over its diagonal such that $\tilde{\mathbf{x}}_q = \boldsymbol{\Theta}_q \mathbf{x}_q$. For ease of notation, from now on we will consider the matrix $\boldsymbol{\Theta}_q$ included in the measurement matrix $\mathbf{A}_q$. The details regarding the estimation of $\boldsymbol{\Theta}_q$ will be discussed in the next section. Accordingly, with reference to (6), our first variable is $\mathbf{x} \in \mathbb{R}^{QN\times 1}$ containing the magnitude of all local images $\mathbf{x} = \{\mathbf{x}_q\}_{q=1}^{Q}$, and the second variable represents the magnitude of the global image $\mathbf{x}_\mathbf{G}$. Consequently, our objective function contains $f(\mathbf{x}) = \sum_{q=1}^{Q} \|\mathbf{y}_q - \mathbf{A}_q\mathbf{x}_q\|_2^2$ and $g(\mathbf{x}_\mathbf{G}) = \|\mathbf{x}_\mathbf{G}\|_1$.

In the sequel, we will provide our proposed aforementioned formulations and their solutions in terms of variable updates according to (8).

A. Consensus ADMM (CADMM)

As the name suggests, by posing the problem according to this formulation, we pursue a solution that, at optimum, provides a sparse global image on which all clusters reach a consensus. While the paper deals with anisotropic settings, we present CADMM as an initial work towards introducing distributed optimization for imaging applications. Consequently, the constraints, in this case, are defined to impose this relationship between the global and local images. Additionally, as mentioned earlier and by following our paper [29], we impose

the l_1-norm function to promote sparse global image solution. The problem becomes

$$\begin{aligned} \underset{\mathbf{x},\mathbf{x_G}}{\arg\min} \quad & \sum_{q=1}^{Q} \frac{\mu}{2} \left\| \mathbf{y}_q - \mathbf{A}_q \mathbf{x}_q \right\|_2^2 + \lambda \left\| \mathbf{x_G} \right\|_1 \\ s.t. \quad & \mathbf{x}_q - \mathbf{x_G} = \mathbf{0} \quad \forall q. \end{aligned} \tag{9}$$

where λ and μ are positive hyperparameters set to penalize less sparse global image solutions and trade-off the data fidelity term, respectively. Note that the Q constraints in (9) can be written in the form of the constraint in (6) by having $\mathbf{G} = \mathbf{I}_{QN}$, $\mathbf{u} = \mathbf{x}$, $\mathbf{H} = -[\mathbf{I}_N, \mathbf{I}_N, \cdots \mathbf{I}_N]^T$ of the size $QN \times N$, $\mathbf{z} = \mathbf{x_G}$, and $\mathbf{c} = \mathbf{0}$ of size $QN \times 1$.

As indicated in (8), the solution of (9) can be obtained by alternately minimizing its associated augmented Lagrangian with respect to $\mathbf{x}$, $\mathbf{x_G}$, and the dual variable $\boldsymbol{\sigma}$. The augmented Lagrangian is

$$\mathcal{L}\left(\mathbf{x}, \mathbf{x_G}, \boldsymbol{\sigma}\right) = \left\{ \begin{array}{c} \sum_{q=1}^{Q} \left\{ \frac{\mu}{2} \left\| \mathbf{y}_q - \mathbf{A}_q \mathbf{x}_q \right\|_2^2 + \left\langle \boldsymbol{\sigma}_q, \mathbf{x}_q - \mathbf{x_G} \right\rangle \right\} \\ + \frac{\beta}{2} \left\| \mathbf{x}_q - \mathbf{x_G} \right\|_2^2 + \lambda \left\| \mathbf{x_G} \right\|_1 \end{array} \right\}, \tag{10}$$

where $\boldsymbol{\sigma}_q \in \mathbb{R}^{N \times 1}$ is the sub-vector of the dual variable $\boldsymbol{\sigma} \in \mathbb{R}^{QN \times 1}$ which corresponds to the local image $\mathbf{x}_q$.

The resulting updates of each variable according to CADMM formulation are provided hereinafter in detail.

1) Update of $\mathbf{x}$ (Local Images): Let ${\mathbf{x_G}}^{(k)}$ and $\boldsymbol{\sigma}^{(k)}$ denote the values of $\mathbf{x_G}$ and $\boldsymbol{\sigma}$ after the k^{th} iteration. Since $\mathcal{L}\left(\mathbf{x}, \mathbf{x_G}, \boldsymbol{\sigma}\right)$ in (10) is decomposable with respect to $\mathbf{x}_q$, the updated $\mathbf{x}^{(k+1)}$ can be obtained by updating all local images $\mathbf{x}_q^{(k+1)}$ for $q = 1, \ldots, Q$ in parallel as

$$\begin{aligned} \mathbf{x}_q^{(k+1)} &= \underset{\mathbf{x}_q}{\arg\min}\, \mathcal{L}\left(\mathbf{x}_q; {\mathbf{x_G}}^{(k)}, \boldsymbol{\sigma}_q^{(k)}\right) \\ &= \underset{\mathbf{x}_q}{\arg\min} \left\{ \begin{array}{c} \frac{\mu}{2} \left\| \mathbf{y}_q - \mathbf{A}_q \mathbf{x}_q \right\|_2^2 + {\boldsymbol{\sigma}_q^{(k)}}^T \mathbf{x}_q \\ + \frac{\beta}{2} \left\| \mathbf{x}_q - {\mathbf{x_G}}^{(k)} \right\|_2^2 \end{array} \right\}, \end{aligned} \tag{11}$$

The problem in (11) is differentiable with respect to $\mathbf{x}_q$ and the $(k+1)^{\text{th}}$ update can be obtained in a closed-form by letting $\nabla_{\mathbf{x}_q} \mathcal{L} = \mathbf{0}$ resulting in

$$\mathbf{x}_q^{(k+1)} = \left(\mu \mathbf{A}_q^H \mathbf{A}_q + \beta \mathbf{I}_N\right)^{-1} \left(\mu \mathbf{A}_q^H \mathbf{y}_q + \beta {\mathbf{x_G}}^{(k)} - \boldsymbol{\sigma}_q^{(k)}\right), \tag{12}$$

Note that the inverse in (12) is possible since $\left(\mu \mathbf{A}_q^H \mathbf{A}_q + \beta \mathbf{I}_N\right)$ is a positive definite matrix.

2) Update of $\mathbf{x_G}$ (Global Image): For the global image update, following the ADMM framework, we consider

$$\begin{aligned} \mathbf{x_G}^{(k+1)} &= \underset{\mathbf{x_G}}{\arg\min}\, \mathcal{L}\left(\mathbf{x_G}; \mathbf{x}^{(k+1)}, \boldsymbol{\sigma}^{(k)}\right) \\ &= \underset{\mathbf{x_G}}{\arg\min} \left\{ \begin{array}{c} \lambda \left\| \mathbf{x_G} \right\|_1 + \sum_{q=1}^{Q} {\boldsymbol{\sigma}_q^{(k)}}^T \mathbf{x_G} \\ + \frac{\beta}{2} \sum_{q=1}^{Q} \left\| \mathbf{x}_q^{(k+1)} - \mathbf{x_G} \right\|_2^2 \end{array} \right\}. \end{aligned} \tag{13}$$

This objective function above involves information from all Q clusters and is not decomposable with respect to $\mathbf{x_G}$. It further involves a non-differentiable function $\left\| \mathbf{x_G} \right\|_1$. Thus, it can neither be parallelized nor solved in a closed form like (11). As a result, it is more suitable for the global image update to be carried out in a central processor after collecting local updates calculated at the distributed clusters. Moreover, for the subsequent update of local images, the global image needs to be broadcast to all the clusters. Alternatively, if the global image update were to be carried out at distributed clusters, a fully meshed communication network would be needed to exchange all local updates among the Q clusters. Later in Section III-C, we will show how to solve (13) in the central node.

3) Update of $\boldsymbol{\sigma}$ (Dual Variable): After updating the global image, the dual variable can be updated by

$$\boldsymbol{\sigma}^{(k+1)} = \boldsymbol{\sigma}^{(k)} + \beta \left(\mathbf{x}^{(k+1)} - \mathbf{1}_Q \otimes \mathbf{x_G}^{(k+1)}\right), \tag{14}$$

The Kronecker product is used to replicate the global image to the same size as the vectors $\mathbf{x}$ and $\boldsymbol{\sigma}$. Since (14) is decomposable, it can be carried out in parallel as well as local images' updates. Instead, it is more convenient for the dual variable to be updated in the central node subsequent to the update of global images. Then, both updates are broadcast to the distributed clusters for the next update of local images.

B. Sharing ADMM (SADMM)

Under this formulation, we impose a different constraint on the optimization problem to explore a different relationship between the local images and the global image. The constraint is set such that the reconstructed global image is the sparse average of all local images. Accordingly, the problem becomes

$$\begin{aligned} \underset{\mathbf{x},\mathbf{x_G}}{\arg\min} \quad & \sum_{q=1}^{Q} \frac{\mu}{2} \left\| \mathbf{y}_q - \mathbf{A}_q \mathbf{x}_q \right\|_2^2 + \lambda \left\| \mathbf{x_G} \right\|_1 \\ s.t. \quad & \bar{\mathbf{x}} - \mathbf{x_G} = \mathbf{0} \end{aligned} \tag{15}$$

where $\bar{\mathbf{x}} = \sum_{q=1}^{Q} \mathbf{x}_q$ contains the sum of magnitudes of local images. Note that the size of constraints is reduced to the size of a single image instead of Q images in the consensus formulation. The nomenclature stems from the constraint above since the global image is considered a shared combination of all local images. We can again write the constraint of (15) in the form of the constraint in (6) by having $\mathbf{G} = [\mathbf{I}_N, \mathbf{I}_N, \cdots \mathbf{I}_N]$ of size $N \times QN$, $\mathbf{u} = \mathbf{x}$, $\mathbf{H} = -\mathbf{I}_N$, $\mathbf{z} = \mathbf{x_G}$, and $\mathbf{c} = \mathbf{0}$.

The augmented Lagrangian of (15) can then be written as

$$\mathcal{L}\left(\mathbf{x}, \mathbf{x_G}, \boldsymbol{\sigma}\right) = \left\{ \begin{array}{c} \sum_{q=1}^{Q} \frac{\mu}{2} \left\| \mathbf{y}_q - \mathbf{A}_q \mathbf{x}_q \right\|_2^2 + \lambda \left\| \mathbf{x_G} \right\|_1 \\ + \left\langle \boldsymbol{\sigma}, \bar{\mathbf{x}} - \mathbf{x_G} \right\rangle + \frac{\beta}{2} \left\| \bar{\mathbf{x}} - \mathbf{x_G} \right\|_2^2 \end{array} \right\}. \tag{16}$$

Note that since the number of constraints is reduced, the dual variable $\boldsymbol{\sigma}$ has a size $N \times 1$ instead of $QN \times 1$ as in CADMM. Next, we provide the variable updates according to the SADMM formulation.

1) Update of $\mathbf{x}$ *(Local Images):* Unlike the consensus case, the augmented Lagrangian function (16) is not directly decomposable into Q terms because of the variable $\bar{\mathbf{x}}$ inside the augmented quadratic term which contains the sum of local images. However, we show here that it is still possible to solve for each local image variable $\mathbf{x}_q$ in parallel. Similar to (11), we use the values of $\mathbf{x}_{\mathbf{G}}^{(k)}$ and $\boldsymbol{\sigma}_q^{(k)}$ in order to solve for $\mathbf{x}_q$ at the $(k+1)^{\text{th}}$ iteration. However, since we have also $\bar{\mathbf{x}}$ in (16), we keep the values of all other local images ($\mathbf{x}_i^{(k)}\ \forall i \neq q$) fixed. Let $\bar{\mathbf{x}}_q^{(k)} = \sum_{(i\neq q)} \mathbf{x}_i^{(k)} = \bar{\mathbf{x}}^{(k)} - \mathbf{x}_q^{(k)}$. Consequently, the q^{th} local image update can be obtained by

$$\begin{aligned}\mathbf{x}_q^{(k+1)} &= \arg\min_{\mathbf{x}_q} \mathcal{L}\left(\mathbf{x}_q; \bar{\mathbf{x}}_q^{(k)}, \mathbf{x}_{\mathbf{G}}^{(k)}, \boldsymbol{\sigma}^{(k)}\right) \\ &= \arg\min_{\mathbf{x}_q} \left\{ \begin{array}{c} \frac{\mu}{2}\left\|\mathbf{y}_q - \mathbf{A}_q\mathbf{x}_q\right\|_2^2 + {\boldsymbol{\sigma}^{(k)}}^T\mathbf{x}_q \\ +\frac{\beta}{2}\left\|\mathbf{x}_q + \bar{\mathbf{x}}_q^{(k)} - \mathbf{x}_{\mathbf{G}}^{(k)}\right\|_2^2 \end{array} \right\} \\ &= \arg\min_{\mathbf{x}_q} \left\{ \begin{array}{c} \frac{\mu}{2}\left\|\mathbf{y}_q - \mathbf{A}_q\mathbf{x}_q\right\|_2^2 + {\boldsymbol{\sigma}^{(k)}}^T\mathbf{x}_q \\ +\frac{\beta}{2}\left\|\mathbf{x}_q + \bar{\mathbf{x}}^{(k)} - \mathbf{x}_q^{(k)} - \mathbf{x}_{\mathbf{G}}^{(k)}\right\|_2^2 \end{array} \right\}\end{aligned} \tag{17}$$

Now similar to (11), the problem in (17) is fully differentiable with respect to $\mathbf{x}_q$ and the $(k+1)^{\text{th}}$ update can be obtained in the closed-form

$$\mathbf{x}_q^{(k+1)} = \left(\mu\mathbf{A}_q^H\mathbf{A}_q + \beta\mathbf{I}_N\right)^{-1}\left(\mu\mathbf{A}_q^H\mathbf{y}_q + \beta\left(\mathbf{x}_{\mathbf{G}}^{(k)} - \bar{\mathbf{x}}_q^{(k)}\right) - \boldsymbol{\sigma}^{(k)}\right). \tag{18}$$

From (18), we can observe that in SADMM, the q^{th} local image update requires the previous state $\mathbf{x}_q^{(k)}$, the sum of the previous updates of all other local images $\bar{\mathbf{x}}^{(k)}$, the global image update $\mathbf{x}_G^{(k)}$, and the dual variable update $\boldsymbol{\sigma}_q^{(k)}$. This suggests the need for extra memory with respect to CADMM to track the previous state at each cluster. Additionally, the distributed clusters will need to receive each other updates. This can be broadcast by the central node subsequent to the update of the global image and dual variables. The central node will have such values regardless since they are needed for the global image update. Although the exchanged information between the central node and the distributed clusters in SADMM seems to be more than CADMM, the size of those variables to be exchanged is still less than CADMM by a factor of $(Q+2)/3$ due to the reduced size of the dual variable in SADMM. This significantly reduces communication bandwidth requirements between the central node and the sensors, especially for a large number of distributed sensors.

2) Update of $\mathbf{x}_{\mathbf{G}}$ *(Global Image):* Similar to the global image update in Section III-A, after collecting the updates of the local image from the distributed sensors, the global image update for the sharing formulation is obtained by minimizing the augmented Lagrangian with respect to $\mathbf{x}_{\mathbf{G}}$ as follows

$$\mathbf{x}_{\mathbf{G}}^{(k+1)} = \arg\min_{\mathbf{x}_{\mathbf{G}}} \left\{\lambda\left\|\mathbf{x}_{\mathbf{G}}\right\|_1 + \tfrac{\beta}{2}\left\|\mathbf{x}_{\mathbf{G}} - \bar{\mathbf{x}}^{(k+1)}\right\|_2^2 + {\boldsymbol{\sigma}^{(k)}}^T\mathbf{x}_{\mathbf{G}}\right\}. \tag{19}$$

Again, we here assume that both the global image and the dual variable are calculated at the central node. As a result, the sum of the local images $\bar{\mathbf{x}}^{(k)}$ is calculated directly at the central node following the local updates collection needed for the global image update. The solution of (19) will be detailed in Section III-C.

3) Update of $\boldsymbol{\sigma}$ *(Dual variable):* The dual variable update then is a straightforward step of the ADMM algorithm

$$\boldsymbol{\sigma}^{(k+1)} = \boldsymbol{\sigma}^{(k)} + \beta\left(\bar{\mathbf{x}}^{(k+1)} - \mathbf{x}_{\mathbf{G}}^{(k+1)}\right) \tag{20}$$

Deferring the study of the imaging performance of each formulation to the next section, it suffices to summarize that SADMM provides an alternative processing architecture with respect to CADMM in which: 1) extra memory is needed at the distributed clusters for local image updates, 2) communication overhead between the distributed clusters and the central node is reduced by a factor of $(Q+2)/3$ due to the difference in the size of the constraints. In both CADMM and SADMM, local images can be updated in parallel at each cluster node and communicated back to the central node. The central node in turn updates both the global image and the dual variable. Subsequently, both the global image and dual variable updates are broadcast back to the distributed clusters in the case of CADMM in addition to the sum of the previous local images in the case of SADMM in order to calculate the next local image updates. Other comparisons and performance metrics such as image reconstruction quality and convergence rate will be provided later in Section IV.

C. Solution Techniques

Considering the above formulations, in this section, we provide the techniques used to solve the sub-problems for local images and global image updates. Additionally, we provide the stopping criteria adopted to terminate both algorithms. Lastly, we show how to obtain the phases of complex-valued local images prior to ADMM iterations.

1) Variable Updates: The updates of local images (12) and (18), employ a matrix inversion in a closed-form solution. However, due to the large size of the problem, it needs to be solved iteratively using a numerical procedure. In particular, we carry out the inversion in the local update using the conjugate gradient (CG) method [36]. Being a numerical method, the output of CG is a complex-valued image since both the measurements $\mathbf{y}_q$ and the forward model $\mathbf{A}_q$ are complex. However, the optimization is carried out over the real-valued magnitude of the images where the phase of the images is included in the measurement matrix. Therefore, subsequent to the update of the local image using CG, a projection of the resulting complex image on the real positive orthant is applied to obtain the magnitude of the local image. This projection implicitly states that the phase of the complex-valued output of CG is regarded as a numerical phase error.

On the other hand, global image updates, (13) and (19), require solving a LASSO-like optimization problem which can be solved using a proximal gradient method. In our numerical experiments, we used the accelerated proximal gradient [37] to calculate the global image updates.

2) Stopping Criteria: Variable updates are repeated until termination which is decided upon comparing the values of the primal and dual residuals with their corresponding feasibility tolerances ϵ_{pri} and ϵ_{dual}, respectively.

Following the definitions of the residuals and the stopping criteria brought up in [24], let $\boldsymbol{\eta}_{pri}$ and $\boldsymbol{\eta}_{dual}$ denote the primal and dual residuals, respectively. The dual residual is defined over the subsequent updates of the global image variable. Hence, it is the same for both CADMM and SADMM. Accordingly, at the k^{th} iteration, the dual residual for both formulations is given by

$$\boldsymbol{\eta}_{dual}^{(k)} = \beta \left(\mathbf{x}_{\mathbf{G}}^{(k+1)} - \mathbf{x}_{\mathbf{G}}^{(k)} \right). \tag{21}$$

On the other hand, the primal residual measures the constraint satisfaction and takes a different form in the two formulations. For CADMM, the primal residual is given by

$$\boldsymbol{\eta}_{pri}^{(k)} = \mathbf{x}^{(k+1)} - \mathbf{1}_Q \otimes \mathbf{x}_{\mathbf{G}}^{(k+1)}. \tag{22}$$

Similarly, in SADMM the primal residual is

$$\boldsymbol{\eta}_{pri}^{(k)} = \bar{\mathbf{x}}^{(k+1)} - \mathbf{x}_{\mathbf{G}}^{(k+1)}. \tag{23}$$

The feasibility tolerances can be chosen based on an absolute tolerance ϵ_{abs} and a relative tolerance ϵ_{rel}. Similar to the primal and dual residuals, the feasibility tolerances indicate non-identical definitions depending on the formulation due to the different constraints. In CADMM, they are given by

$$\begin{aligned} \epsilon_{pri} &= \sqrt{QN}\ \epsilon_{abs} + \epsilon_{rel}\ \max\left\{ \left\| \mathbf{x}^{(k)} \right\|_2, \sqrt{Q} \left\| \mathbf{x}_{\mathbf{G}}^{(k)} \right\|_2 \right\} \\ \epsilon_{dual} &= \sqrt{QN}\ \epsilon_{abs} + \epsilon_{rel} \left\| \boldsymbol{\sigma}^{(k)} \right\|_2. \end{aligned} \tag{24}$$

Likewise, for SADMM, feasibility tolerances are

$$\begin{aligned} \epsilon_{pri} &= \sqrt{N}\ \epsilon_{abs} + \epsilon_{rel}\ \max\left\{ \left\| \bar{\mathbf{x}}^{(k)} \right\|_2, \left\| \mathbf{x}_{\mathbf{G}}^{(k)} \right\|_2 \right\} \\ \epsilon_{dual} &= \sqrt{N}\ \epsilon_{abs} + \epsilon_{rel} \left\| \boldsymbol{\sigma}^{(k)} \right\|_2. \end{aligned} \tag{25}$$

Lastly, for both CADMM and SADMM, the algorithm is terminated either when a defined maximum number of iterations is reached or when both the ensuing inequalities are satisfied

$$\begin{aligned} \left\| \boldsymbol{\eta}_{pri}^{(k)} \right\|_2 &\leqslant \epsilon_{pri} \\ \left\| \boldsymbol{\eta}_{dual}^{(k)} \right\|_2 &\leqslant \epsilon_{dual}, \end{aligned} \tag{26}$$

where the variables in the above inequalities are calculated according to the definitions of the corresponding quantities (21)-(25).

3) Phase Matrix $\boldsymbol{\Theta}$: As mentioned earlier, we assume that the phase of local images is already provided prior to carrying out the optimization algorithms. Our proposed imaging methods can be considered partially non-coherent imaging methods since the phases are only used within the data-fidelity term in the objective function. Thus, a coarse estimated phase of local images is sufficient for our algorithms to perform satisfactorily. Therefore, we use the phase of the images obtained by backprojection for each cluster as an estimate of the phase of local images. Accordingly, for each cluster q, the diagonal matrix containing the phase of all pixels of its local image is constructed as

$$\boldsymbol{\Theta}_q = \text{diag}\left\{ \exp\left(j[\angle(\mathbf{A}_q^H \mathbf{y}_q)] \right) \right\}. \tag{27}$$

Finally, a summary of the steps of CADMM and SADMM is reported in Algorithm 1.

Algorithm 1 Widely Distributed Radar Imaging using CADMM and SADMM

Input:

- The measurement matrices $\{\mathbf{A}_q\}_{q=1}^{Q}$
- Measured echos signal $\{\mathbf{y}_q\}_{q=1}^{Q}$
- Hyperparameters μ and β
- Absolute and relative tolerances ϵ_{abs} and ϵ_{rel}

Initialize:

- Local images $\left\{ \hat{\mathbf{x}}_q^{(0)} = \mathbf{0} \right\}_{q=1}^{Q}$
- Global image $\hat{\mathbf{x}}_{\mathbf{G}}^{(0)} = \mathbf{0}$
- Dual variable $\boldsymbol{\sigma}^{(0)} = \mathbf{0}$
- The iteration counter $k = 0$

while stopping criterion (26) not satisfied **do**

1) Update $\left\{ \hat{\mathbf{x}}_q^{(k+1)} \right\}_{q=1}^{Q}$ locally in parallel
   - CADMM $\rightarrow$ (12)
   - SADMM $\rightarrow$ (18)
2) Update $\hat{\mathbf{x}}_{\mathbf{G}}^{(k+1)}$ in central node
   - CADMM $\rightarrow$ (13)
   - SADMM $\rightarrow$ (19)
3) Update $\left\{ \boldsymbol{\sigma}_q^{(k+1)} \right\}_{q=1}^{Q}$ in central node
   - CADMM $\rightarrow$ (14)
   - SADMM $\rightarrow$ (20)
4) $k \leftarrow k + 1$.

end while

Output: $\hat{\mathbf{x}}_{\mathbf{G}}$

IV. Performance Evaluation

In this section, we validate and evaluate the performance of the algorithms proposed in Section III to reconstruct radar images using distributed sensor clusters. To achieve this goal, we use the publicly available Civilian Vehicle Dome (CV Domes) dataset which offers simulated scattering data of civilian vehicle facet models. Although the dataset is originally intended to simulate circular synthetic aperture radars, a particular configuration of WSAR, it can also be used to simulate a mono-static distributed radar sensors system.

First, we give a brief introduction to the dataset and its parameters. Consequently, we define the performance metrics used in our evaluation to compare both algorithms. Finally, we evaluate our algorithms on three different scenarios of practical relevance for several applications. The scenarios are realized by different combinations of full/limited views and full/limited bandwidth measurements as we will show later in this section.

A. Data-set Introduction

CV Domes dataset contains simulated electromagnetic high-frequency scattering data of ten civilian vehicles. For each model, an X-band mono-static scattering is simulated in a far-field scenario. Scattered waves are simulated with full polarization over an azimuth extent of $360°$ where 16 viewing angles per degree of azimuth are considered. Similarly, data are simulated over the range of elevation angles from $30°$ to $60°$. For each tuple of azimuth and elevation viewing angles, 512 frequency samples of complex-valued scattering coefficients centered at 9.6 GHz and spanning a bandwidth of approximately 5.35 GHz are provided. The range information of those frequency measurements is compressed already resulting in what is usually referred to as phase history.

B. Performance Metrics

As discussed in the previous section, the difference in problem formulation between CADMM and SADMM has induced slightly different system implementation features in terms of memory requirements and communication bandwidth. Additionally, to compare the performance of the proposed algorithms, the following aspects are considered.

1) Convergence rate: it can be assessed by the number of iterations needed to reach the stopping criteria that is defined identically for both algorithms.
2) Computational complexity: the main computational burden of both algorithms lies in the local image updates (12) and (18), where the matrix inversion term is present. Due to their large size, the measurement matrices $\mathbf{A}_q$ are realized through matrix operators based on two-dimensional non-uniform Fast Fourier transform (2D NuFFT) [38]. Moreover, the inversion step is carried out numerically using CG as mentioned earlier. Thus, while the complexity of both algorithms seems to be equivalent, the convergence of CG highly depends on the other variables in the update formulas (12) and (18). As a result, the comparison solely in terms of the number of iterations is not indicative since a single iteration in each of the algorithms may realize a different cost. Accordingly, computational complexity can be measured by calculating the total processing time spent until termination.
3) Image reconstruction quality: the dataset does not contain a reference image with which a comparison can be made in order to evaluate the quality of reconstructed images. Correspondingly, we use image entropy as a quantitative metric to assess the image quality being a measure of its sharpness or constituent randomness. The smaller the image entropy the sharper the reconstructed image and vice versa. After clipping the image intensity values which are beyond a certain dynamic range in the dB scale, the image is translated to the grayscale so the entropy is calculated in bits. Consequently, a randomly generated image would have an entropy equal to or close to 8 bits. Additionally, as a subjective measure of image quality, the images reconstructed utilizing full aperture and full bandwidth measurement could act as a visual reference for the other scenarios when the aperture and/or the bandwidth measurements are reduced.

C. Experiments

In this subsection, we demonstrate the imaging results of CADMM and SADMM using the simulated data of two different vehicle models differing in type and geometry. The first is of a Jeep Cherokee (SUV) 'Jeep99', while the second is of a Toyota Tacoma (Pick-up) 'Tacoma'. We consider image reconstruction utilizing the dataset according to the following scenarios:

1) Full aperture views measurements: for a general validation of both algorithms, the full $360°$ aperture measurements of the entire available bandwidth is considered.
2) Full views and limited bandwidth measurements: limited frequency samples of the full aperture measurements are considered for image reconstruction realizing a typical use case of WSAR imaging.
3) Limited views and limited bandwidth measurements: assuming a distributed system of radar sensors illuminating the scene according to a time division multiplexing (TDM) scheme, limited frequency samples of limited aperture measurements are considered for image reconstruction.

For all experiments, measurements are taken at a fixed elevation angle of $30°$ and with 'HH' polarization. Moreover, all measurements are impaired with a white Gaussian noise realizing a signal-to-noise ratio (SNR) of 15 dB. A fine grid of 256 cells in both range and cross-range directions (7 meter-long each) is used resulting in a total number of $N = 65536$ pixels. Additionally, images are reconstructed considering an elevated image plane at 1 meter from the ground level. This renders the projection of layover-ed elements to be mostly contained within the vehicle's outlines and permits a better visual interpretation.

The choice of μ, β, and λ for both CADMM and SADMM is made through a parameter sweep guided by normalized image sparsity and image entropy as performance metrics. The normalized sparsity considered is the percentage of the non-zero pixels in the image. Hyperparameters used to reconstruct the illustrated images throughout this section are those that guarantee a similar degree of sparsity for both CADMM and SADMM images at a lower entropy value. Also, we tried to pick the parameters where β is as close as possible in both methods for a fair comparison of convergence rates. Given the considered scene size and typical dimensions of a vehicle, a sparsity level around the range of $5\% - 10\%$ is considered in our experiments based on the scenario and the vehicle. Needless to say, parameter sweep analysis is conducted separately for each dataset and each scenario. It is worth mentioning that, for a given β, the ratio λ/μ can be automatically selected given the desired sparsity range following our method proposed in [39]. However, since for both CADMM and SADMM an empirical search for β is needed and at almost exact sparsity levels, a parameter sweep would facilitate finding more accurate parameters for the sake of comparison. An example of image sparsity and image

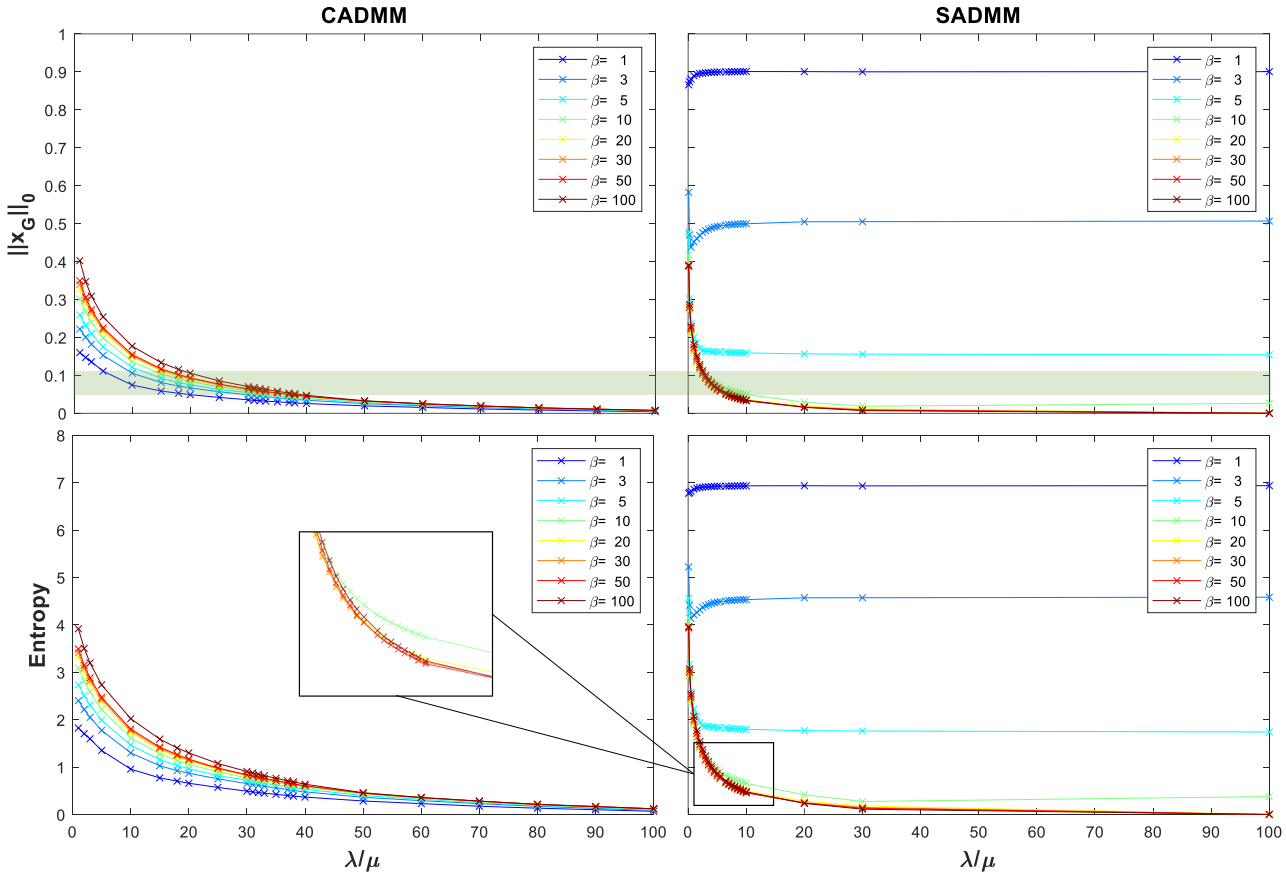

Fig. 2: Hyperparameters sweep for 'Jeep99' data (FVFB); normalized sparsity (top row), image entropy (bottom row)

entropy versus different parameters is shown for the first scenario. For later experiments, such analysis will be omitted for brevity. CADMM and SADMM are run for a maximum number of 100 iterations while the feasibility tolerances ϵ_{abs} and ϵ_{rel} are both set to 10^{-2}. Scenario-specific parameters and reconstructed images of all the aforementioned experiments are provided and discussed in the sequel.

1) Full Views - Full Bandwidth (FVFB): Using the full 360° azimuth extent and the full bandwidth of the dataset (approximately equal to 5.35 GHz), we reconstruct the images of the two vehicles to validate our proposed methods and show their superior reconstruction quality with respect to the conventional BP method. The reconstructed images in this experiment can also be used as a reference for subsequent scenarios when images are reconstructed using limited views and/or limited bandwidth measurements. As mentioned previously, to avoid anisotropic scattering over the large angular azimuth extent, it is divided into sub-apertures (clusters) at which the isotropic scattering assumption is valid. The angular width of a cluster has a double-faced effect on the imaging performance trading-off between angular resolution and homogeneous target scattering. The wider the cluster the better the resolution while the scattering becomes anisotropic. Therefore, in this experiment, the cluster width is chosen to maximize the imaging performance in a balanced manner. We use a cluster width of 5° withing which we assume the targets exhibit isotropic scattering.

As anticipated earlier, we perform a hyperparameter sweep over different values of β and λ/μ to obtain the values that provide good reconstruction quality given the image sparsity level. The sparsity level is decided based on the assumed dimensions of the observed targets relative to the scene dimensions. They are set separately for each scenario due to the dissimilarities of aperture size and signal bandwidth utilized, hence images exhibit a different resolution in each scenario. Fig. 2 shows the normalized sparsity level and entropy of the reconstructed image of the 'Jeep99' dataset versus the varying parameters of β and λ/μ for both SADMM and CADMM. The desired sparsity level range is highlighted with a light green color in the figure. As expected, the higher the ratio λ/μ, the more sparse the reconstructed images for both the algorithms and naturally the lower the entropy. This is true except for some values of β for which SADMM optimization does not converge to a sparse solution. Such divergence for those parameters can be seen from the entropy values which indicate the reconstruction of random images. Moreover, beyond those values of β, reconstructed images using the same λ/μ ratio exhibit similar sparsity levels and attain close values for entropy as shown in the magnified part of Fig. 2.

To first demonstrate the performance of both methods,

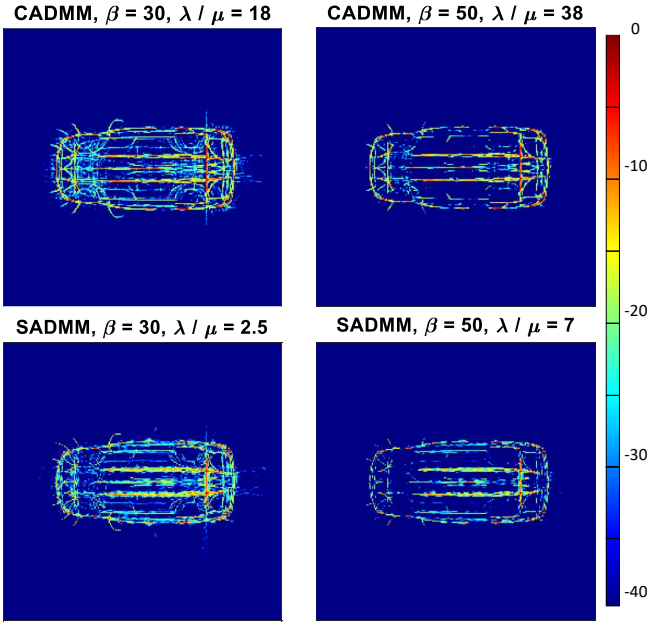

Fig. 3: Jeep image reconstruction at different sparsity levels; 12% (left column), 5% (right column)

CADMM and SADMM images reconstructed considering two different sparsity levels are shown for the 'Jeep99' dataset in Fig. 3. The left column images have a normalized sparsity degree of 12% versus 5% for the images in the right column. For lower sparsity images, CADMM shows a sharp high-intensity reconstruction of the strong features of the vehicle such as edges and ceiling structure, and a lower intensity reconstruction of the weaker features such as the projection of the tire wheels. On the other hand, SADMM images manifest an averaged intensity of the different parts of the vehicle resulting in less sharp images. While the behavior is maintained for the images at higher sparsity, the weaker features are further suppressed in the images of both methods. Moreover, the images of both methods at a similar sparsity level have similar entropy values. This behavior is again confirmed by the reconstructed images of the 'Tacoma' vehicle. At a sparsity level of 10%, the reconstructed images of the two vehicles are shown in Fig. 4 in addition to the images reconstructed through conventional back-projection averaged over all clusters. The red dots on the images show the angular aperture views which cover $360°$ in this experiment. Note that due to the abundance of the available bandwidth and the full aperture measurements, both CADMM and SADMM images have very high resolution and show the detailed structure of the imaged objects.

Additionally, the processing time until termination in SADMM is higher than CADMM. The numerical values of the parameters used in image reconstruction and the corresponding metrics are reported in Table I while the ratio between SADMM and CADMM processing time and number of iterations are reported in Table II.

2) Full Views - Limited Bandwidth (FVLB): In practice, the signal bandwidth of a SAR system is usually an order of

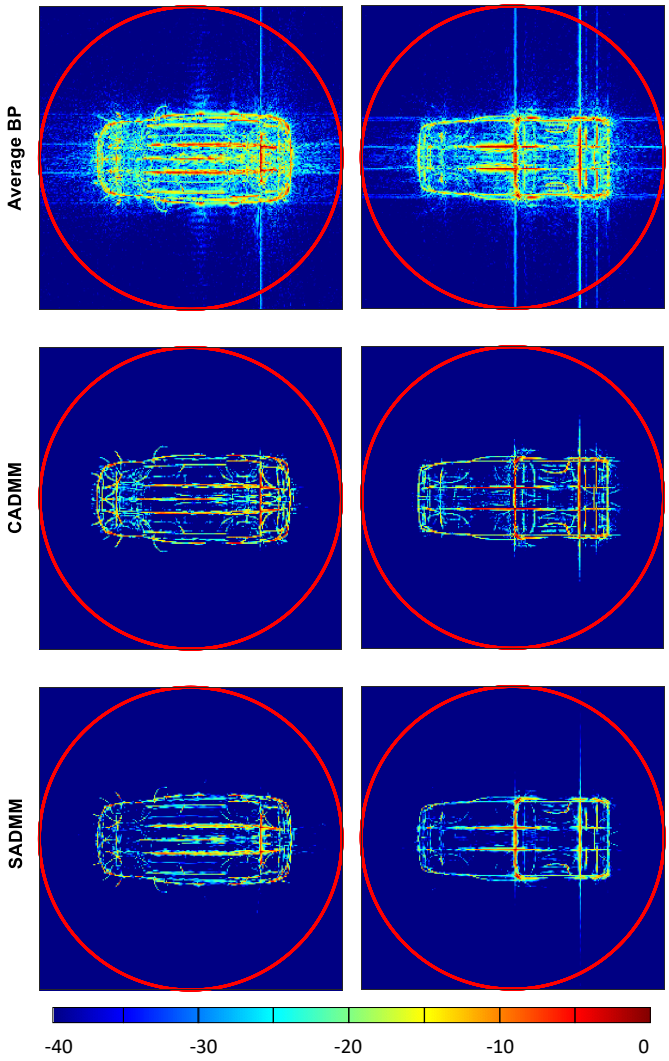

Fig. 4: FVFB image reconstruction at sparsity level $\approx 10\%$, $Q = 72$ clusters, bandwidth $= 5.35$ GHz; Jeep Cherokee (left column), Toyota Tacoma (right column)

magnitude less than the available bandwidth of the dataset. Thus, analyzing the performance of our proposed algorithms considering fewer bandwidth samples is of high interest and is a relevant use case in WSAR imaging. To realize a limited bandwidth measurement scenario, we utilized an equivalent of 600 MHz samples around the center frequency from the samples of phase history. In this experiment as well, SADMM images exhibit the property of higher averaging than that of concentrated intensity resulting from CADMM images as shown in Fig. 5. This peculiarity makes it capable of capturing the true structure of the vehicles even with low bandwidth measurements when referring to the images in Fig. 4 of FVFB experiment. On the other hand, images reconstructed using CADMM have higher intensity around the strong reflectors and weaker or no intensity of the poorly reflective components of the vehicles; this is evident in the reconstructed images of both vehicles in Fig. 5. For example, the crossing of the

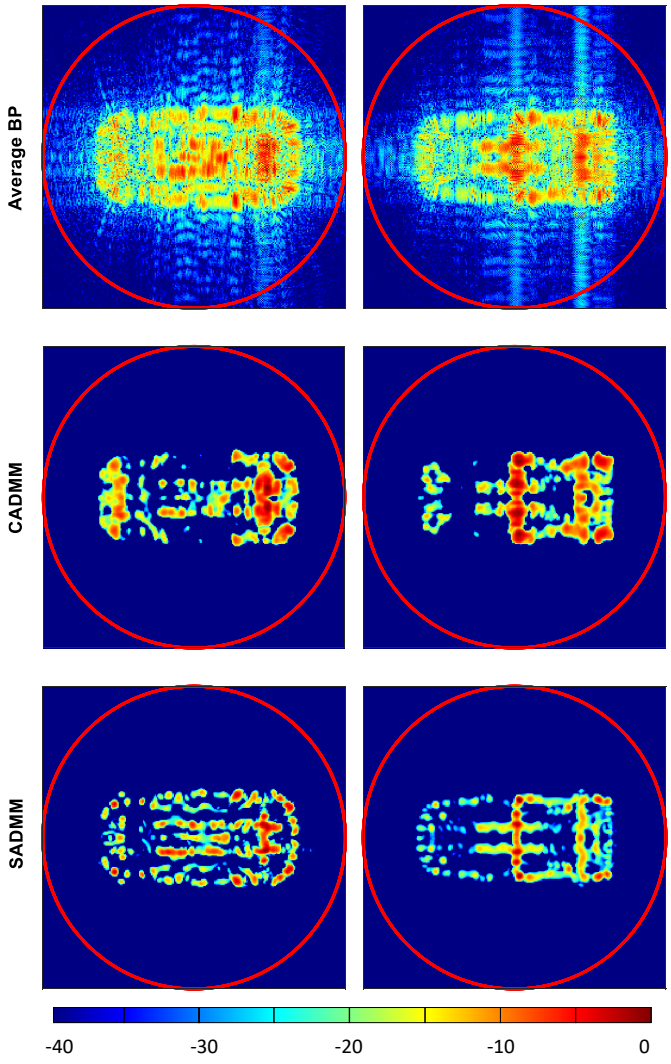

Fig. 5: FVLB image reconstruction at sparsity level $\approx 10\%$, $Q = 72$ clusters, bandwidth $= 600$ MHz; Jeep Cherokee (left column), Toyota Tacoma (right column)

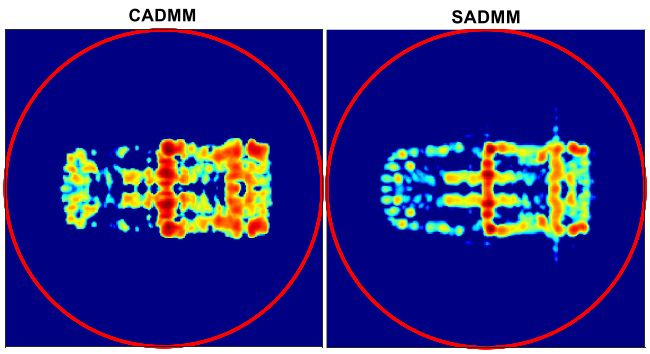

Fig. 6: Less sparse FVLB reconstruction of Toyota Tacoma (sparsity level $\approx 15\%$).

beams in the rear part of the 'Jeep99' data is localized and well identified with strong intensity in the SADMM image, while in the CADMM image, the same area exhibits only a strong intensity in a wider region. Similarly, in 'Tacoma' images, CADMM fails to capture the outline of the vehicle at this sparsity level and the image is dominated by the strong trunk while in SADMM image the vehicle outline makes an appearance and even the trunk is better identified. The depicted images have a sparsity level approximately equal to 10%. Note that by considering lower sparsity, images of both algorithms will increase the background intensity around the strong features without capturing the general structure of the object differently. An example is shown in Fig. 6 where the images of the 'Tacoma' vehicle are reconstructed at a lower normalized sparsity level of about 15%. In summary, although CADMM images have similar entropy values as their SADMM counterparts at the same sparsity level, the latter provides a higher capability of capturing the structure of the observed targets given relatively low bandwidth measurements. The exact values of sparsity and entropy for each image are reported in Table I.

The superior performance of SADMM comes at the cost of increased computational complexity to reach convergence. This complexity is manifested through the higher number of iterations and the longer processing time required for SADMM to reconstruct the shown images. The ratio of these two quantities for SADMM and CADMM is depicted in Table II.

3) Limited views - Limited Bandwidth (LVLB): A monostatic distributed sensing scenario can be realized by considering far-field illumination with limited and narrow views of the full aperture measurements. In this experiment, we consider using the dataset to realize a system of distributed radar sensors in which the TDM scheme is used to illuminate the scene of interest where a single cluster transmits at a time. Consequently, in addition to the limited bandwidth measurements of 600 MHz introduced in the previous experiment, we further consider limited aperture measurements representing the views of distributed sensors. In particular, 16 clusters of 1° width each are uniformly distributed around the scene and considered as the viewing angles of the sensors. This number of clusters makes a realistic choice for the number of sensors where they cover only a span of about 4.4% of the full aperture measurements.

For this experiment, the reconstructed images of the two vehicles are shown in Fig. 7. Similar to the previous experiment, SADMM captures both vehicles' structures better than CADMM. However, due to the limited aperture measurements, the artifacts present in the images of both methods are stronger. Increasing the sparsity would eliminate the artifacts but further limit the reconstruction of the entire outline of the vehicles.

Of course, reconstructed images are view-dependent. However, the performance of both methods is the same when the different orientation of the sensors is considered. For example, the images reconstructed using another random orientation of views are shown in Fig. 8. The images confirm the capability of SADMM to retain the original structure of the imaged target while CADMM has a better ability to diminish the artifacts. Similar to previous experiments, processing times for imaging using SADMM are higher than the time needed

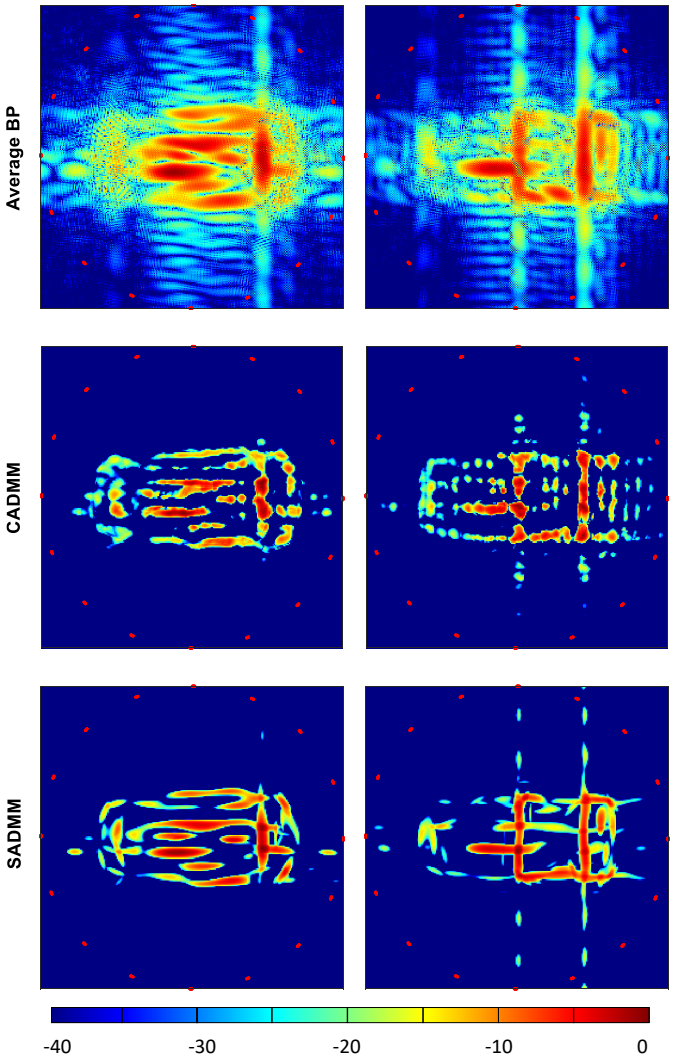

Fig. 7: LVLB image reconstruction at sparsity level $\approx 10\%$, $Q = 16$ clusters, bandwidth $= 600$ MHz; Jeep Cherokee (left column), Toyota Tacoma (right column)

for CADMM. Finally, the parameters used to reconstruct the images in Fig. 7 and the corresponding values of entropy and sparsity are reported in Table I while processing time and the number of iterations ratios are reported in Table II.

Finally, to provide an additional comparison with the state-of-the-art, we reconstructed the images of 'Jeep99' using LS-CS-Residual composite imaging [22]. Fig. 9 depicts the performance of the LS-CS-Residual composite imaging in the three scenarios combining different aperture and bandwidth ranges. Comparing with the results of CADMM and SADMM in Figs. 4, 5 and 7, shows the limitations of using the methods of DCS and/or methods that rely on the evolution of RCS when the support of the underlying image sequence is not highly overlapped as the case of the dataset we use. This is particularly evident in the scenarios of limited views and/or limited bandwidth, where LS-CS-Residual imaging almost fails completely.

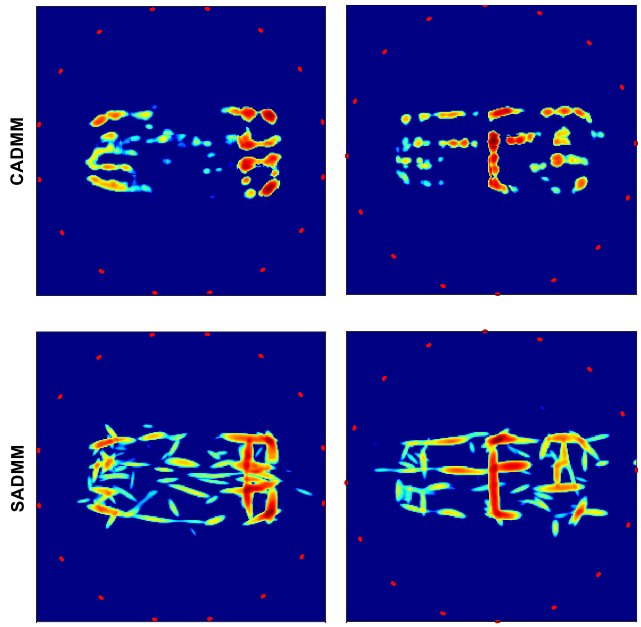

Fig. 8: LVLB reconstruction with different random sensors orientation; Jeep Cherokee (left column), Toyota Tacoma (right column)

Additionally, since in LS-CS-Residual imaging the update of each local image depends on the estimate of the preceding image in the sequence, the implementation is forced to be sequential. This is another advantage of our proposed methods where local images can be updated in parallel at each iteration. This is further highlighted by the significantly contrasted computing times of our proposed method versus LS-CS-Residual which are reported in Table III. The reported values serve also as an indication of the absolute computing time of our proposed methods, in addition to the relative values reported in Table II. All numerical experiments were carried out on a node of the High-Performance Computing (HPC) facility at the University of Luxembourg [40]. The node utilized has AMD EPYC 7H12 64-Core processor CPU at 2.6 GHz and 256 GB of physical memory and is running a MATLAB Version: R2021a. By leveraging a multi-core processor, we implemented both CADMM and SADMM to run local updates in parallel but were not able to realize a similar implementation for LS-CS-Residual composite imaging.

To summarize, in the first experiment where a plenitude of measurements in both aperture and bandwidth is available, both CADMM and SADMM are capable of reconstructing detailed and super-resolution images of the observed targets far surpassing the conventional methods. On the other hand, in the latter experiments where measurements are limited in aperture and/or bandwidth, SADMM exhibits superior performance over CADMM in terms of capturing the structure of the target and reconstructing smoother images. Although they have similar entropy in all cases, the depicted images reconstructed by both algorithms show a clear visual advantage of SADMM by reference to the images of full measurements. Such higher quality comes at the expense of higher

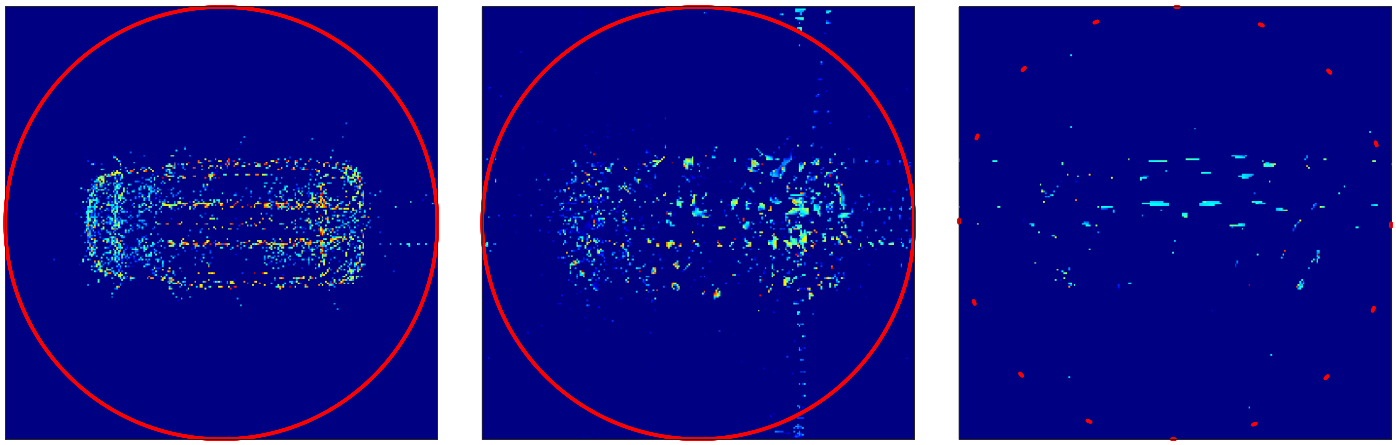

Fig. 9: LS-CS-Residual imaging results for 'Jeep99' data for the three experiments; FVFB (left), FVLB (middle), LVLB (right).

TABLE I: Summary of parameters used in the experiments and corresponding metrics

		FVFB		FVLB		LVLB	
		CADMM	SADMM	CADMM	SADMM	CADMM	SADMM
$(\beta,\ \lambda/\mu)$	Jeep	(30,18)	(30,2.5)	(30,16)	(30,1.4)	(10,1.25)	(20,0.4)
	Tacoma	(30,25)	(30,2.5)	(30,24)	(50,1.8)	(10,1.75)	(20,0.65)
Sparsity	Jeep	0.100	0.102	0.104	0.102	0.100	0.098
	Tacoma	0.096	0.10	0.097	0.098	0.099	0.103
Entropy	Jeep	1.24	1.25	1.27	1.26	1.25	1.22
	Tacoma	1.19	1.24	1.20	1.21	1.24	1.26

TABLE II: Relative convergence and complexity

	FVFB		FVLB		LVLB	
Ratio SADMM/CADMM	Number of iterations	Processing time	Number of iterations	Processing time	Number of iterations	Processing time
Jeep	1.41	1.46	3.45	2.11	1.45	2.19
Tacoma	1.41	1.52	3.13	2.06	1.51	2.04

TABLE III: Absolute computing times using proposed methods vs. LS-CS-Residual for 'Jeep99' (minutes)

	FVFB	FVLB	LVLB
CADMM	5.1562	1.2264	0.4066
SADMM	7.5389	2.5879	0.8902
LS-CS-Residual	21.1528	16.1970	3.9681

computational costs. Surprisingly, in terms of convergence and complexity, SADMM fell behind the most in the second experiment where the full aperture measurements with limited bandwidth are considered. This can be owed to the fact that SADMM has fewer degrees of freedom than CADMM which with the full aperture measurements requires less than a third of SADMM iterations to reach convergence.

V. Conclusion

In this paper, a novel approach for widely distributed radar-induced synthetic aperture imaging based on the ADMM framework is proposed. Sparsity prior has been imposed on a defined global image assumed to represent an aggregate view of the scene. Then, developing on top of our previous work, the problem formulation is tailored to this approach and a new formulation has been introduced. The two formulations named CADMM and SADMM are designed to mathematically stipulate the relationship between the images of individual sensors and the defined global image. The solutions to the proposed formulations have been provided as iterative algorithms that are flexible and amenable to be implemented on a distributed architecture. We have demonstrated the performance of our proposed algorithms through several experiments and showed their significant edge over conventional methods in terms of reconstructed image quality. Moreover, we showed that SADMM outperforms CADMM by reconstructing images of high resolution that better exhibit the structure and the shape of the observed objects, especially when the measurements are limited in bandwidth and/or sparse in aperture. As we illustrated in our experiments, our proposed algorithms are

applicable in many scenarios of distributed radar systems and WSAR imaging. Following our approach, various formulations can be further studied and developed either by imposing different prior on the global image and/or by imposing alternative associations with the images of the individual sensors.

REFERENCES

[1] A. M. Haimovich, R. S. Blum, and L. J. Cimini, "Mimo radar with widely separated antennas," *IEEE Signal Processing Magazine*, vol. 25, no. 1, pp. 116–129, 2007.

[2] P. Vouras and et.al, "An overview of advances in signal processing techniques for classical and quantum wideband synthetic apertures," *arXiv, submitted 11 May 2022*.

[3] S. Z. Gurbuz and M. G. Amin, "Radar-based human-motion recognition with deep learning: Promising applications for indoor monitoring," *IEEE Signal Processing Magazine*, vol. 36, no. 4, pp. 16–28, 2019.

[4] G. Gennarelli, F. Soldovieri, and M. Amin, "Radar for indoor surveillance: state of art and perspectives," in *Multimodal Sensing: Technologies and Applications*, vol. 11059. International Society for Optics and Photonics, 2019.

[5] R. L. Moses, L. C. Potter, and M. Cetin, "Wide-angle SAR imaging," in *Algorithms for Synthetic Aperture Radar Imagery XI*, vol. 5427. International Society for Optics and Photonics, 2004, pp. 164–175.

[6] M. A. Lodhi, H. Mansour, and P. Boufounos, "Coherent radar imaging using unsynchronized distributed antennas," in *IEEE International Conference on Acoustics, Speech and Signal Processing (ICASSP)*, 2019, pp. 4320–4324.

[7] H. Mansour, D. Liu, U. Kamilov, and P. Boufounos, "Sparse blind deconvolution for distributed radar autofocus imaging," *IEEE Transactions on Computational Imaging*, vol. 4, pp. 537–551, 2018.

[8] H. Mansour, D. Liu, P. T. Boufounos, and U. S. Kamilov, "Radar autofocus using sparse blind deconvolution," in *IEEE International Conference on Acoustics, Speech and Signal Processing (ICASSP)*. IEEE, 2018, pp. 1623–1627.

[9] J. Ash, E. Ertin, L. C. Potter, and E. Zelnio, "Wide-angle synthetic aperture radar imaging: Models and algorithms for anisotropic scattering," *IEEE Signal Processing Magazine*, vol. 31, no. 4, pp. 16–26, 2014.

[10] L. C. Potter and R. L. Moses, "Attributed scattering centers for sar atr," *IEEE Transactions on Image Processing*, vol. 6, no. 1, pp. 79–91, 1997.

[11] M. Liu, B. Zhang, Z. Xu, and Y. Wu, "Efficient parameter estimation for sparse SAR imaging based on complex image and azimuth-range decouple," *Sensors*, vol. 19, no. 20, p. 4549, 2019.

[12] N. Sugavanam and E. Ertin, "Interrupted SAR imaging with limited persistence scattering models," in *2017 IEEE Radar Conference (RadarConf)*, 2017-05, pp. 1770–1775, ISSN: 2375-5318.

[13] Y. Yang, G. Gui, R. Hu, X. Zhang, X. Cong, and Q. Wan, "Robust polarimetric sar imaging method with attributed scattering characterization," *IEEE Access*, vol. 7, pp. 52 414–52 426, 2019.

[14] G. B. Hammond and J. A. Jackson, "Sar canonical feature extraction using molecule dictionaries," in *2013 IEEE Radar Conference (RadarCon13)*. IEEE, 2013, pp. 1–6.

[15] R. Hu, R. Min, and Y. Pi, "A video-SAR imaging technique for aspect-dependent scattering in wide angle," *IEEE Sensors Journal*, vol. 17, no. 12, pp. 3677–3688, 2017.

[16] T. Sanders, A. Gelb, and R. B. Platte, "Composite SAR imaging using sequential joint sparsity," *Journal of Computational Physics*, vol. 338, pp. 357–370, 2017.

[17] Z. Wei, L. Yang, Z. Wang, B. Zhang, Y. Lin, and Y. Wu, "Wide angle SAR subaperture imaging based on modified compressive sensing," *IEEE Sensors Journal*, vol. 18, no. 13, pp. 5439–5444, 2018.

[18] Z. Xu, M. Liu, G. Zhou, Z. Wei, B. Zhang, and Y. Wu, "An accurate sparse SAR imaging method for enhancing region-based features via nonconvex and TV regularization," *IEEE Journal of Selected Topics in Applied Earth Observations and Remote Sensing*, vol. 14, pp. 350–363, 2021.

[19] J. Ziniel and P. Schniter, "Dynamic Compressive Sensing of Time-Varying Signals Via Approximate Message Passing," *IEEE Transactions on Signal Processing*, vol. 61, no. 21, pp. 5270–5284, Nov. 2013.

[20] N. Vaswani, "LS-CS-Residual (LS-CS): Compressive Sensing on Least Squares Residual," *IEEE Transactions on Signal Processing*, vol. 58, no. 8, pp. 4108–4120, Aug. 2010.

[21] N. Vaswani and J. Zhan, "Recursive Recovery of Sparse Signal Sequences From Compressive Measurements: A Review," *IEEE Transactions on Signal Processing*, vol. 64, no. 13, pp. 3523–3549, Jul. 2016.

[22] Z. Wei, B. Zhang, and Y. Wu, "Accurate wide angle SAR imaging based on LS-CS-residual," *Sensors (Basel, Switzerland)*, vol. 19, no. 3, p. 490, 2019.

[23] T. Scarnati and A. Gelb, "Accurate and Efficient Image Reconstruction from Multiple Measurements of Fourier samples," *Journal of Computational Mathematics*, vol. 5, no. 38, p. 797, Mar. 2021.

[24] S. Boyd, N. Parikh, and E. Chu, *Distributed Optimization and Statistical Learning Via the Alternating Direction Method of Multipliers*. Now Publishers Inc, 2011.

[25] M. V. Afonso, J. M. Bioucas-Dias, and M. A. T. Figueiredo, "Fast image recovery using variable splitting and constrained optimization," *IEEE Transactions on Image Processing*, vol. 19, no. 9, pp. 2345–2356, 2010.

[26] ——, "An augmented lagrangian approach to the constrained optimization formulation of imaging inverse problems," *IEEE Transactions on Image Processing*, vol. 20, no. 3, pp. 681–695, 2011.

[27] H. Guven, A. Gungor, and M. Çetin, "An augmented lagrangian method for complex-valued compressed SAR imaging," *IEEE Transactions on Computational Imaging*, vol. 2, pp. 235–250, 2016.

[28] A. Güngör, M. Çetin, and H. E. Güven, "Autofocused compressive sar imaging based on the alternating direction method of multipliers," in *2017 IEEE Radar Conference (RadarConf)*, 2017, pp. 1573–1576.

[29] R. Hu, B. S. Mysore Rama Rao, A. Murtada, M. Alaee-Kerahroodi, and B. Ottersten, "Widely-distributed radar imaging based on consensus ADMM," in *2021 IEEE Radar Conference (RadarConf21)*, 2021, pp. 1–6, ISSN: 2375-5318.

[30] K. E. Dungan, C. Austin, J. Nehrbass, and L. C. Potter, "Civilian vehicle radar data domes," in *Algorithms for Synthetic Aperture Radar Imagery XVII*, vol. 7699, 2010, p. 76990P.

[31] D. C. Munson, J. D. O'brien, and W. K. Jenkins, "A tomographic formulation of spotlight-mode synthetic aperture radar," *Proceedings of the IEEE*, vol. 71, no. 8, pp. 917–925, 1983.

[32] H.-T. Tran and L. L. Monte, "Radar tomography," pp. 141–187, Nov. 2019, publisher: IET Digital Library.

[33] C. V. Jakowatz, D. E. Wahl, P. H. Eichel, D. C. Ghiglia, and P. A. Thompson, *Spotlight-Mode Synthetic Aperture Radar: A Signal Processing Approach*. Boston, MA: Springer US, 1996.

[34] H. Griffiths and C. Baker, "Fundamental of tomography and radar," Jan. 2006, pp. 171–187.

[35] M. Çetin, Ö. Önhon, and S. Samadi, "Handling phase in sparse reconstruction for SAR: Imaging, autofocusing, and moving targets," in *EUSAR 2012; 9th European Conference on Synthetic Aperture Radar*, 2012, pp. 207–210.

[36] J. R. Shewchuk *et al.*, "An introduction to the conjugate gradient method without the agonizing pain," 1994, publisher: Carnegie-Mellon University. Department of Computer Science.

[37] A. Beck and M. Teboulle, "A fast iterative shrinkage-thresholding algorithm for linear inverse problems," *SIAM journal on imaging sciences*, vol. 2, no. 1, pp. 183–202, 2009.

[38] J. Fessler and B. Sutton, "Nonuniform fast fourier transforms using min-max interpolation," *IEEE Transactions on Signal Processing*, vol. 51, no. 2, pp. 560–574, 2003.

[39] A. Murtada, R. Hu, M. Alaee-Kerahroodi, U. Schroeder, and B. Shankar M. R., "Efficient radar imaging using partially synchronized distributed sensors," in *2021 IEEE Radar Conference (RadarConf21)*, pp. 1–6.

[40] S. Varrette, P. Bouvry, H. Cartiaux, and F. Georgatos, "Management of an academic hpc cluster: The ul experience," in *Proc. of the 2014 Intl. Conf. on High Performance Computing & Simulation (HPCS 2014)*. Bologna, Italy: IEEE, July 2014, pp. 959–967.